

**GT2021-59285**

## CORRELATING CAVITY SEALING EFFECTIVENESS TO TIME-RESOLVED RIM SEAL EVENTS IN THE PRESENCE OF VANE TRAILING EDGE FLOW

**Shawn Siroka, Iván Monge-Concepción, Reid A. Berdanier,**  
**Michael D. Barringer, and Karen A. Thole**  
 The Pennsylvania State University  
 Department of Mechanical Engineering  
 University Park, PA 16802, USA

**Christopher Robak**  
 Pratt & Whitney, a division of  
 Raytheon Technologies Corporation  
 East Hartford, CT 06118, USA

### ABSTRACT

The cavity region between the rotor and stator relies on hardware seals and purge flow to discourage hot gas path air from being ingested into the unprotected wheel space. However, ingestion can occur due to a combination of disk pumping, periodic vane-blade interactions, and three-dimensional seal geometry effects. These mechanisms create flow instabilities that are detrimental to cavity seal performance under certain conditions. In this paper, a one-stage turbine operating at engine representative conditions was utilized to study the effect of steady and time-resolved under-platform cavity temperatures and pressures across a range of coolant flow rates in the presence of vane trailing edge (VTE) flow. This study correlates time-resolved pressure with time-resolved temperature to identify primary frequencies driving ingestion. At certain flow rates, the time-resolved pressures are out of phase with the temperatures, indicating ingestion. These same flow rates were found to correlate to an inflection region in the cooling effectiveness curve where the maximum amplitude of the time-varying behavior coincides with the cooling effectiveness inflection point. Using a time-accurate computational model, simulations near this inflection region illustrate ingestion of high-swirl VTE flow into the cavity region which creates a buffer in the rim seal between swirled main gas path flow and axially injected purge coolant helping to suppress the amplitude of time-resolved behavior.

### NOMENCLATURE

$b$	Hub radius
$c$	CO <sub>2</sub> concentration
$C_p$	Pressure Coefficient ( $(P-P_{\text{mean}})/(0.5\rho\Omega_D^2b^2)$ )
$C_{x,B}$	Blade axial chord length
$f$	Frequency
$\dot{m}$	Mass flowrate
$P$	Pressure

$P_v$	Vane Pitch
$PR$	Turbine Pressure Ratio
$r$	Radius
$Re_x$	Axial Reynolds number, $Re_x = U_{\text{rel}} C_{x,B} \nu^{-1}$
$Re_\Omega$	Rotational Reynolds number, $Re_\Omega = \Omega_D b^2 \nu^{-1}$
$s_c$	Seal clearance
$T$	Temperature
$t$	Time
$U_{\text{rel}}$	Relative velocity
$V$	Voltage
$V_\phi$	Circumferential velocity
$X$	Arbitrary variable

### Greek

$\alpha$	Angular distance between pressure sensors
$\beta$	Swirl ratio, $\beta = V_\phi r^{-1} \Omega_D^{-1}$
$\Delta$	Change in quantity
$\Gamma$	Ratio of cavity discharge coefficients
$\varepsilon_{cc}$	Cooling effectiveness $(c-c_{\text{MGP}})/(c_s-c_{\text{MGP}})$
$\theta$	Cavity cooling efficiency $(T_{\text{MGP}}-T)/(T_{\text{MGP}}-T_p)$
$\nu$	Kinematic viscosity
$\rho$	Density
$\Phi$	Nondimensional flow rate $\dot{m}/(2\pi s_c \rho \Omega_D b^2)$
$\Phi_0$	$\Phi$ relating to initial increase in $\varepsilon_{cc}$
$\Phi^*$	Net nondimensional flow rate $(\Phi - \Phi_0)$
$\Psi$	Arbitrary phase shift
$\Psi_T$	Phase shift from $C'_{p1}$ to $T'$
$\Psi_p$	Phase shift from $C'_{p1}$ to $C'_{p2}$
$\Omega$	Angular speed

### Subscripts and Accents

$*$	Normalized over all test conditions
$'$	Normalized over a single test condition
$1$	Related to first pressure sensor

2	Related to second pressure sensor
D	Related to the disk
ex	Excitation voltage
max	Maximum quantity
min	Minimum quantity
MGP	Main gas path quantity
o	Stagnation property
p	Purge flow quantity
ref	Reference condition
rs	Related to rim seal
VTE	Related to vane trailing edge flow

## INTRODUCTION

As lofty goals are targeted by the aviation industry to reduce emissions [1], greater efficiency is required for gas turbine engines. One of the driving factors of efficiency is the turbine entry temperature. For several decades, this parameter has surpassed the softening temperature of the turbine components [2] creating durability challenges in the downstream parts.

One area particularly affected by the harsh environment is the turbine cavity region between rotating and stationary components. This region is designed to seal the unprotected wheel space from hot gas path ingestion. Although many types of seals exist, most aviation engines discourage ingress through a combination of various axial and radial clearance changes. The outermost seal where the platform of the blade and platform of the vane overlap is often referred to as the rim seal. Rim seals are subject to ingestion because of their proximity to the main gas path. For that reason, measurements in the rim seal are the main focus of this paper. Secondary air from the compressor is injected at a low radius to pressurize the cavity. Because this bleed air causes a penalty to the efficiency of the engine, it is imperative to develop an understanding of the physical mechanisms that drive the ingestion and ensure effective use of secondary air.

Attempts to understand and predict the sealing effectiveness of first stage turbine cavities through computational modeling are powerful, yet limited. Because this region is a low-potential three-dimensional flow field with time-varying vane-blade interactions, models are either computationally expensive or oversimplified. Under certain flow conditions where the time-varying pressure field drives ingress, such models often result in inaccurate predictions [3,4]. As a result, there is a need for time-resolved measurements to develop time-accurate models and understand how to control and manage these flow behaviors.

This paper utilizes a one-stage turbine with engine-representative hardware and seal geometries to provide a time-resolved dataset linking pressure and temperature events to the steady cooling effectiveness in the rim seal cavity. First, the impact of vane trailing edge (VTE) flow on steady cavity performance is analyzed. Then, the time-resolved pressure and temperature are correlated indicating a connection between coolant flowrates and time-varying ingress. This ingress is further examined through spectral decomposition using VTE flow to investigate how pressure asymmetries around the annulus affect instabilities in the cavity region. Finally, a

computational model is utilized to augment the experimental data by tracking VTE flow ingestion and changes in cavity dynamics with and without VTE flow present.

## LITERATURE REVIEW

A plethora of literature exists on cavity ingestion mechanisms. Johnson et al. [5] outlines several mechanisms in a holistic review article of cavity ingestion including: disk pumping, periodic vane and blade pressure fields, 3-D geometric effects, asymmetries in the rim seal, turbulent transport, and flow entrainment. The more recent literature has focused on the sealing effectiveness parameter,  $\epsilon$ , for various types of seals [6]. The sealing effectiveness is an important parameter in cavity performance because it provides a direct quantification of the ingress of the main gas path flow through concentration measurements of a tracer gas [7]. This literature review will focus on isolating the periodic effects from the blade-vane interaction as well as the time-varying flow instabilities that can arise in the cavity region. Particular focus will be placed on how the time-varying flow can influence the sealing effectiveness.

The majority of studies conducted to date compare cavity sealing performance with an analytical model [8–10]. One established model for sealing effectiveness by Sangan et al. [11,12] simplifies the rim seal geometry into a ring with two orifices, one for ingress and one for egress, to develop an analytical relationship. The model accounts for externally-induced ingress, rotationally-induced ingress, and swirl effects in the cavity. However, theoretically-indeterminate empirical constants are needed to solve the effectiveness equations. Because of this, it is difficult to incorporate as a true predictive tool, but its integration provides a valuable relationship with data that is grounded in physics. Although the model by Sangan et al. has been successfully applied in various studies, there are conditions for which the trend predicted by the model cannot fully explain certain behaviors in the sealing effectiveness curve [3,4,13]. The discrepancy between the model and the data in these situations has been attributed to instabilities in the cavity causing increased ingestion [13]. Although these instabilities have been studied, they are not currently well understood.

One possible onset of the time-varying ingress is the asymmetric pressure field from the vane-blade interaction [14]. Bohn et al. [15] studied the effect vanes have on ingress in a single stage turbine rig without blades through pressure and velocity measurements indicative of ingress. Without vanes, results indicate that a fully-sealed condition can occur at high coolant flow rates but with the introduction of wakes from the vane, hot gas path ingestion cannot be completely suppressed. Later, Bohn et al. [14] conducted a supplemental study using CO<sub>2</sub> as a tracer gas to measure the sealing effectiveness of the cavity. In this study, the effect of rotational and blade Reynolds numbers ( $Re_\Omega$  and  $Re_x$ ) on ingestion was investigated for two simple seal designs. Bohn et al. showed that as the blade Reynolds number increased, the ingress also increased due to the larger velocity deficit in the wake of the vane. Bohn et al. [16,17] provided a comprehensive look at the investigation with the

addition of blades. This work concluded that for different seal geometries, the presence of rotor blades could either significantly improve or hinder the sealing performance of the cavity based on relevant geometric parameters and how the blade interacts with the vane wake. Overall, these series of experiments show the large effect the vane wake has on the cavity performance and how blades can create additional impacts on the seal. They also show that the rim seal performance is truly a time-varying behavior that is not effectively characterized through steady evaluation techniques.

In addition to the time-varying vane-blade interaction, large-scale rotating pressure structures in the cavity region have been experimentally measured and numerically predicted [18,19]. These structures are not captured in the orifice model outlined by Sangan et al. [11,12] and may be an additional cause of deviation from predicted trends. Using computational predictions, rotating pressure structures have been found to move at a variety of speeds with a range of cell numbers at frequencies uncoupled to the vane and blade count [20]. Furthermore, structures moving at low frequencies have been shown to exist without blades and vanes, suggesting the cause of the instability is not necessarily externally driven [13,19]. This observation is of particular interest for the present study.

Rabs et al. [21] attributed the presence of large-scale rotating pressure structures to the Kelvin-Helmholtz instability. Kelvin-Helmholtz instabilities are formed in the presence of a velocity shear layer. In a turbine rim seal application, the method of coolant flow injection can play a critical role in determining the velocity shear layer and, hence, the formation of these instabilities. Patinios et al. [22] studied the effect of different coolant injection methods in a single-stage turbine cavity with simplified seals. In this study, Patinios et al. concluded that the coolant injection method has a large impact on the sealing performance of the cavity. Particularly, bore flow cooling (low radius injection) is more effective than purge flow cooling (high radius injection) for a given cavity design. Darby et al. [23], used the same facility to evaluate the effect of angling the purge injection. In the study, co-swirl (direction of the vane exit velocity), contra-swirl (opposite direction of the vane exit velocity), and axial injection were considered. The co-swirl injection method proved to be a much more efficient choice, improving cavity sealing by as much as 15% over the other two for the same flow rate. Darby et al. also showed an inflection present in the sealing effectiveness curve was less pronounced with the co-swirl injection than contra-swirl or axial injection.

Haulca et al. [13] also used the same facility as Darby et al. to study the effect of blades and vanes on ingress in gas turbines. Using a series of fast response pressure transducers, their study concludes the presence of time-resolved pressure events in the cavity are correlated to the inflection point of the sealing effectiveness curve when both vanes and blades are present. These structures were measured to be rotating at the disk speed with a frequency equal to half the blade passing frequency.

Presently, many seal geometries and cooling conditions show good agreement with simplified models, but under certain conditions, a combination of vane-blade interaction and cavity

instabilities cause unpredicted behavior in the sealing effectiveness curve. The current study adds to the collection of work on rim events by building additional understanding of the critical vane-blade interaction through the use of time-resolved measurements in the presence of VTE flow. Unsteady pressure events are correlated to ingress in the cavity by incorporating both high frequency pressure and high frequency temperature sensors. Through the use of vane trailing edge flow, the effect of reducing the vane wake velocity deficit is analyzed and shown to be a key contributor to the strength of cavity instabilities.

## EXPERIMENTAL SETUP

The measurements for this study were collected in the Steady Thermal Aero Research Turbine (START) Lab at the Pennsylvania State University. This single-stage turbine is capable of engine-relevant operating conditions with true-scale engine hardware. The facility houses two 1.1 MW (1500 hp) compressors capable of providing continuous mass flow of 12.2 kg/s (25 lbm/s) at a maximum pressure of 480kPa (70 PSIA) to the test section. An in-line 3.5 MW (4700 hp) natural gas heater is capable of raising and maintaining a gas temperature between 395 K to 672 K (250°F to 750°F).

For the current turbine test section design, three independent coolant lines (supplied by bleed air from one of the compressors) distributed to the VTE flow, purge flow, and tangential on-board injection (TOBI) flow (not used in this study). Each of these lines is independently controlled and metered with a discharge temperature of 273 K (32°F) after passing through a shell-and-tube heat exchanger. A full facility description was presented by Barringer et al. [24] with upgrades to the facility highlighted in Berdanier et al. [3].

### Turbine Operating Point and Instrumentation

The test section for the experiment is shown in Figure 1. The single-stage turbine comprises a true-scale vane and blade representative of a modern aero gas turbine. The work presented in this paper focuses on the rim seal measurement plane denoted in Figure 1 as “time-resolved sensor location” ( $r/b = 0.981$ ). The rim seal in this study is defined from the pre-swirl discourager ( $r/b = 0.958$ ) to the inner diameter of the vane platform ( $r/b = 0.990$ ). The minimum seal clearance,  $s_c$ , is at the interface of the rim seal and main gas path measuring  $s_c/b = 0.1$ . Further details about the cavity geometry is given by Robak et. al [25].

In this study, purge flow enters the cavity axially through a set of 150 circumferentially spaced holes fed by a vane under platform plenum. Because the testbed incorporates true-scale engine hardware, the injected coolant flow can go into the cavity, through the blade’s internal flow path, or radially inward. Understanding this complex flow with engine parts at engine realistic conditions makes this dataset particularly unique.

The vane ring contains engine-run hardware as well as several “doublets” that were additively manufactured through a metal sintering process. Of the additive doublets: two contain internal passageways for low frequency pressure and gas concentration measurements and one is specifically designed for high-frequency measurements of temperature and pressure in the

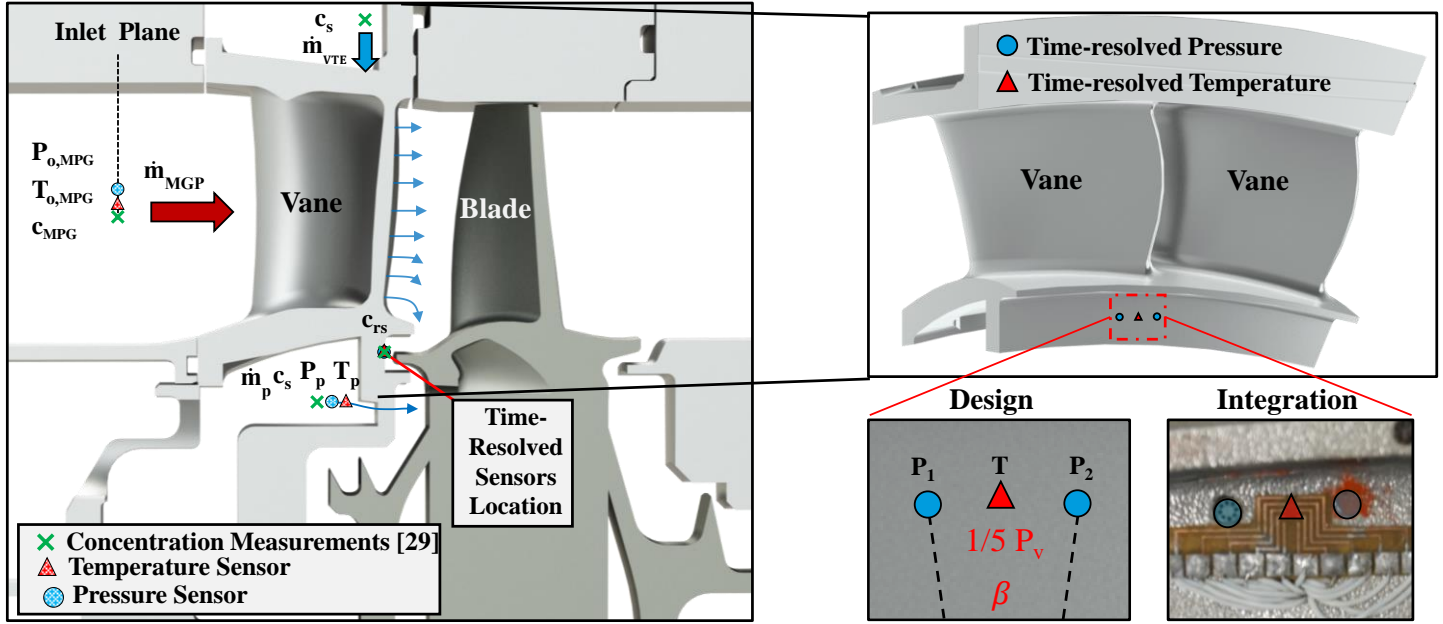


**Figure 1: Diagram of the start test section emphasizing the spatial location of high frequency sensors and their experimental integration.**

rim seal region. All of the vanes include VTE cooling in the form of radially spaced coolant holes spanning from the hub to the tip of the airfoil fed by a plenum radially outboard of the vane ring. Aside from the VTE cooling passages, the vanes and blades in this study operate as uncooled airfoils.

The test section is highly instrumented and the measured quantities relevant to this study are highlighted in Figure 1. The inlet plane total temperature and total pressure are measured through a series of sensors around the annulus approximately eight axial chords upstream of the vane. The main gas path and coolant flows are measured through Venturi flow meters upstream of the test section. Additional pressure and temperature sensors located at the inboard coolant plenum characterize the purge flow. The pertinent turbine operating conditions in this study are located in Table 1. These conditions are maintained over a period of hours as the test section thermally stabilizes. During steady data collection periods, the maximum deviation of specified operating conditions is 0.7% for all parameters listed in Table 1 [26].

**Table 1: Turbine Operating Conditions**

Parameters	Value
Vane Inlet Mach Number	0.1
Vane Inlet Axial Reynolds Number, $Re_x$	$1.1 \times 10^5$
Blade Inlet Axial Reynolds Number, $Re_x$	$1.1 \times 10^5$
Rotational Reynolds Number, $Re_\Omega$	$4.0 - 9.6 \times 10^6$
Density Ratio, $\rho_p/\rho_{MGP}$	1.0 – 2.0
Relative Purge Flow Rate, $\Phi_p/\Phi_{ref}$	0.1 – 1.3
Relative VTE Flow Rate, $\Phi_{VTE}/\Phi_{ref}$	0.0 & 0.4

This study compares the time-resolved measurements to cooling effectiveness measurements for an identical seal geometry previously outlined for the same test article [26]. The turbine operating conditions between this study and Monge-Concepción et al. [26] are set identical for data comparison. In Monge-Concepción et al., a CO<sub>2</sub> tracer gas was systematically added to various cooling flows to get the relative contribution from the VTE flow and the purge flow to the cavity cooling effectiveness,  $\varepsilon_{cc}$  given in Equation 1 as

$$\varepsilon_{cc} = \frac{c_{rs} - c_{MGP}}{c_s - c_{MGP}} \quad (1)$$

where  $c_{rs}$  is the CO<sub>2</sub> concentration measurement in the rim seal,  $c_s$  is the CO<sub>2</sub> concentration of the coolant flow, and  $c_{MGP}$  is the concentration at the inlet. This methodology allows a mass-transfer analysis for the combined coolant effectiveness on the cavity. Note that multiple coolant sources contribute to the  $c_s$  term including the VTE and purge flows. The foundation of measurements collected by Monge-Concepción et al. enable the time-resolved pressure and temperature measured in this study to be correlated with cavity cooling effectiveness. Full descriptions of the concentration measurement methods in this testbed have been outlined in previous studies [3,7,26].

### High Frequency Sensor Calibration

This study utilized both high-frequency pressure transducers and high-frequency temperature sensors to quantify time-resolved events. Figure 1, shows the design and integration of the sensors. The two high-frequency pressure transducers were standard piezo-resistive sensors spaced one-fifth  $P_v$  circumferentially. Between the two pressure transducers, a thin film resistive temperature detector was installed. This

temperature sensor was designed and fabricated using nanofabrication infrastructure at Penn State [27]. The signals from both sensors were digitized at a rate of 100kHz, and a common shaft encoder signal was sent to each acquisition device to ensure signal alignment.

The sensors were fully installed with the vane hardware, and then the instrumented vane assembly was calibrated using a custom pressure vessel with hermetic wire egress. The pressure vessel was then situated in a scientific convection oven with a stability rating at 0.2 K for calibration. Additional ports on the pressure vessel permitted installation of a pressure controller line (accuracy of 0.14 kPa) as well as a precision RTD (accuracy of 0.005 K). The temperature and pressure of the system were automatically swept through predetermined setpoints covering the range of thermodynamic states seen through the experiment. To minimize uncertainty in the results, the same sensor leads, excitation channels, and data acquisition channels were matched for calibration and experiment.

Figure 2(a) illustrates the calibration of the high frequency temperature sensor used in this study. Note, this sensor is insensitive to changes in pressure. Figure 2(b) shows the calibration curve for one of the high frequency pressure sensors; these devices are a primary function of pressure with secondary temperature effects. Therefore, a calibration surface was fitted that is both a linear fit with pressure and temperature. If the temperature compensation was not used for the high frequency pressure transducers, an error of  $\pm 5\%$  would have been introduced. To determine the pressure from the surface, the voltage was measured and the temperature was approximated using the nearby high-frequency temperature sensor.

The uncertainty in the low frequency measurements as well as the high frequency measurements were assessed accounting for the bias and precision error from each sensor. Table 2, lists

the uncertainty of calculated parameters presented throughout the remainder of the paper.

**Table 2: Measurement Uncertainties**

Parameters	Total Uncertainty
Main gas path flow rate, $\dot{m}/\dot{m}_{ref}$	$\pm 0.004$
Shaft rotational speed, $\Omega_D/\Omega_{ref}$	$\pm 0.001$
Pressures, $P/P_{ref}$	$\pm 0.001$
Temperatures, $T$	$\pm 0.4$ K
1.0 stage pressure ratio, $PR/PR_{ref}$	$\pm 0.005$
Purge flow rate, $\dot{m}_p/\dot{m}_{p,ref}$	$\pm 0.018$
Cooling effectiveness, $\epsilon_{cc}$	$\pm 0.015$ to $\pm 0.025$
Time Resolved Pressure, $P_{p1,p2}/P_{ref}$	$\pm 0.0035$
Cooling Efficiency, $\theta$	$\pm 0.026$ to $\pm 0.061$
Normalized Cooling Efficiency $\theta^*$	$\pm 0.0057$
Normalized Pressure Coefficient, $C_p^*$	$\pm 0.00005$
Nondimensional Purge Flow Rate, $\Phi_p/\Phi_{ref}$	$\pm 0.018$

## VANE TRAILING EDGE FLOW IMPACT ON CAVITY TEMPERATURE

Previous tracer gas measurements by Monge-Concepción et al. [26] qualitatively showed that VTE flow is ingested into the under-platform wheel space, but the study did not directly quantify the thermal benefit or detriment to the cavity performance. Figure 3 displays both the cooling effectiveness,  $\epsilon_{cc}$  (filled markers) described in the previous section and the thermal efficiency,  $\theta$  (open symbols) of the cavity defined as

$$\theta = \frac{T_{MGP} - T}{T_{MGP} - T_p} \quad (2)$$

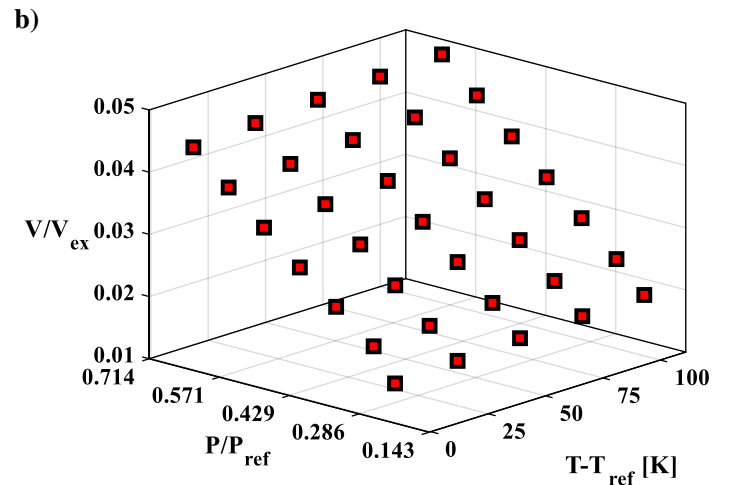
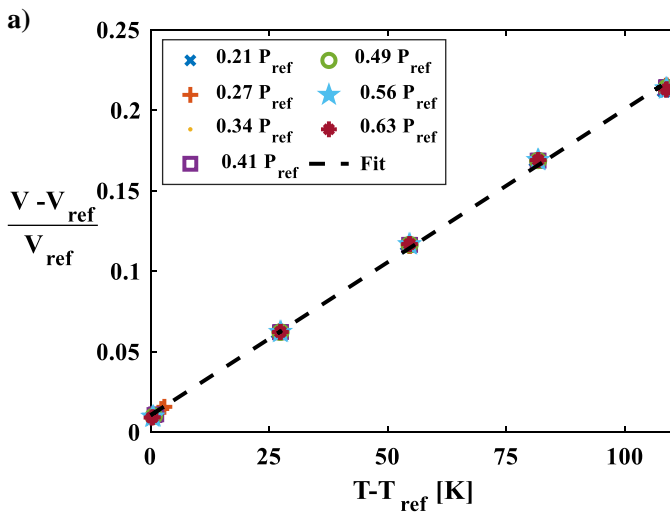


**Figure 2: Example calibration results: a) calibration curve for the high frequency temperature sensor; b) calibration surface for the high frequency pressure transducer.**

where  $T_{MGP}$  is the main gas path temperature,  $T$  is the rim seal vane temperature and  $T_p$  is the purge inlet temperature. These parameters are shown as a function of the nondimensional purge flow rate,  $\Phi_p/\Phi_{ref}$  where  $\Phi_{ref}$  is the nondimensional coolant flow rate required to seal the cavity at the coolant injection plane.  $\Phi_{ref}$  was chosen for consistency with previous studies and serves as a reminder that the radial location of the measurement is integral to the quantification of the sealing effectiveness.

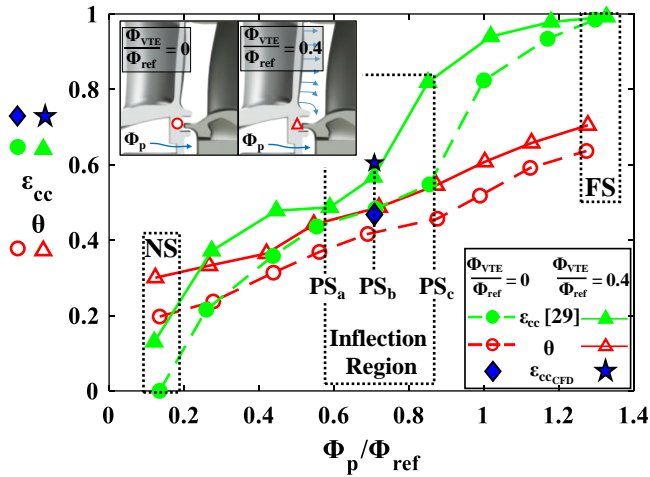


**Figure 3: Thermal efficiency and cooling effectiveness as a function of nondimensional purge flow rates with and without VTE flow.**

The dashed lines in Figure 3 represented cases without VTE flow and the solid lines represent cases with VTE flow. This convention is followed throughout the paper. Figure 3 also denotes several key conditions in dashed boxes that will be referenced throughout the paper. The three main sealing regimes are represented as NS (not sealed), PS (partially sealed), and FS (fully sealed). The partially-sealed region is further divided into three subsections for subsequent comparison: PS<sub>a</sub>, PS<sub>b</sub>, and PS<sub>c</sub>. Accompanying the experimental measurements, Figure 3 contains the CFD predictions for PS<sub>b</sub> with and without VTE flow shown as a star and diamond respectively. Note the agreement between the experiment and computation. These results will be discussed in further detail later.

Several key points are illustrated through Figure 3. First, the presence of VTE flow increases  $\epsilon_{cc}$  for all flow rates tested, as highlighted by Monge-Concepción et al. [26]. This observation independently confirms ingestion of VTE flow into the under-platform region. The presence of the VTE flow acts to cool the cavity across the range of  $\Phi_p/\Phi_{ref}$ , as shown in Figure 3 by an increase in  $\theta$  of 7-10%.

The VTE presence allows two mechanisms to work together to impact the cavity temperature. First, when the coolant flow is injected into the vane, the entire airfoil temperature decreases due to conduction. The conduction path through the vane and into the cavity impacts the thermal efficiency. Second, the additional airflow in the cavity changes the fluid dynamics,

increasing heat transfer by convection. Additionally, this ingested VTE flow displaces hot main gas path flow from being ingested. Although the present study cannot distinguish the individual contributions of the VTE flow, the combined effect demonstrates that cooled turbine designs can accommodate ingress that is not necessarily a detriment – an observation that may be counter to traditional cavity design criteria.

The primary goal of cavity design is to prevent ingress of hot gas path air to keep critical inner radius components cool. Concentration measurements quantify the cavity sealing performance, but must infer how sealing effectiveness relates to cavity temperature. Therefore, a cavity should be quantified by coupling cooling effectiveness measurements with thermal efficiency measurements. This dataset provides that link under a realistic engine configuration. The added benefit of the thermal sensor links ingestion to temperature, more clearly connecting ingestion to component durability.

There is a range of partially-sealed (PS) purge flow rates, denoted in Figure 3 as the inflection region, which should be of particular interest to engine designers. In this region, increasing the coolant flow rate has a minimal impact on the cooling effectiveness of the cavity. This phenomenon has also been identified in previous studies [13,28], and it has been associated with time-varying flow variations in the cavity. Therefore, it is important to understand how the steady cooling effectiveness and thermal efficiency measurements relate to time-varying events.

Furthermore, the addition of VTE flow shifts the onset of this inflection region to higher purge flow rates in Figure 3. This observation suggests that the VTE flow, which affects the vane-blade interaction, also influences ingestion mechanisms. Current cavity effectiveness models [11,12] do not account for external cooling flows, such as VTE flow, nor do they explain the inflection region. Nonetheless, most modern gas turbines include VTE flow to control the velocity deficit created in the vane wake and cool the trailing edge of the vane. Therefore, it is critical to understand both steady and time-resolved interactions of VTE flow with the cavity.

## CORRELATION OF PRESSURE TO TEMPERATURE WAVE PROPOGATION

The time-resolved pressure and temperature measurements allows a methodology of correlating cavity pressure and temperature to ingress. Following this methodology, it is shown that fluidic structures with the largest impact to ingestion are present in the PS region shown in Figure 3.

Figure 4(a) presents normalized temperature,  $T'$ , and normalized pressure coefficient,  $C'_p$ , over one rotor revolution for the partially-sealed case, PS<sub>b</sub>, with VTE flow as shown in Figure 3. This single test condition was chosen to highlight flow features near the inflection region and serves as an example for the analysis. The datasets were normalized by the minimum and maximum of the dataset such that the normalized quantity,  $X'$  is represented as



$$X' = \frac{X - X_{\min}}{X_{\max} - X_{\min}} \quad (3)$$

where  $X$  represents the parameter of interest, such as rim seal vane metal temperature and pressure coefficient. It should be noted that the data presented in this section were filtered during post-processing using a zero-phase low pass digital filter at  $f/f_D = 20$  to remove the blade passing events and other high frequency noise contributions. Through this filtering process, the remaining low-frequency oscillation patterns were identified.

Several significant flow characteristics are shown in the time-resolved pressure and temperature displayed in Figure 4. First, there is a driving frequency at approximately  $f/f_D = 5$  as seen by the five peaks over the rotation in both pressure sensors ( $C'_{p1}$  and  $C'_{p2}$ ) as well as the temperature sensor ( $T'$ ). Second, the temperature and pressure of these peaks are out of phase. The temperature phase lag,  $\Psi_T$ , is defined as the shift of the temperature trace to the pressure trace in degrees and is explicitly called in Figure 4(a).  $\Psi_T$  is an important parameter because it correlates pressure to temperature. Specifically, when the pressure and temperature are out of phase, it indicates time-varying ingress in the cavity. One purpose of the coolant is to pressurize the cavity, sealing it from main gas path ingestion. This means a local maximum of pressure indicative of coolant should coincide with a local minimum in temperature, as shown in Figure 4(a).

Figure 4(b) displays a normalized thermal efficiency and normalized pressure coefficient for the same data as Figure 4(a). All of the traces in Figure 4(b) are in phase because the thermal efficiency of the cavity increases as the high-pressure coolant passes, following the definition of thermal efficiency in Equation 2. When the data are nondimensionalized in this manner, regions of ingress (minima) followed by regions of improved thermal performance (maxima) can be identified from

the sensors in the cavity. These regions of thermal cycling contribute to the time-varying sealing effectiveness in the cavity.

In Figure 4(b), a small phase lag is still present between the pressure signals. This minor phase change corresponds to the angular separation between the two pressure sensors as shown in Figure 1. As the pressure waves propagate, it will contact sensors sequentially in the rotation of the pressure wave movement. Particularly, since the pressure sensors were at known locations, it is possible to get the speed of the cell propagation by calculating the phase shift between pressure sensors,  $\Psi_p$ . Monge-Concepción et al. [29] analyze a dataset similar to the present study to determine the speed and cell count of the time-resolved pressure events and their impact on cavity performance. Although these events could be calculated from the two pressure signals, the phase between the temperature sensor and pressure transducer could not reliably be used to calculate the speed of these cells since the temperature sensors measure the conduction through the part as well as the convection at the surface. The presence of these pressure cells (instabilities) is referenced throughout the current paper, although it is not the primary focus of this study.

To further quantify  $\Psi_T$ , a spectral analysis was performed. A total of 18 different test conditions over a range of flow rates were analyzed, and each dataset contained approximately 500 revolutions. The spectral analysis included an iterative zero padding routine with a convergence criterion of 0.1% of the maximum normalized peak value to ensure consistent peak resolution between cases. From this spectral pressure analysis, peaks were selected such that any normalized peak with an amplitude greater than 1% of the mean value was chosen as a potential driver of ingestion. Using the phase information contained in the spectral analysis,  $\Psi_T$  can then be calculated for those peak frequency values. Figure 5(a-c) outlines these steps in the analysis for the same dataset shown in Figure 4.

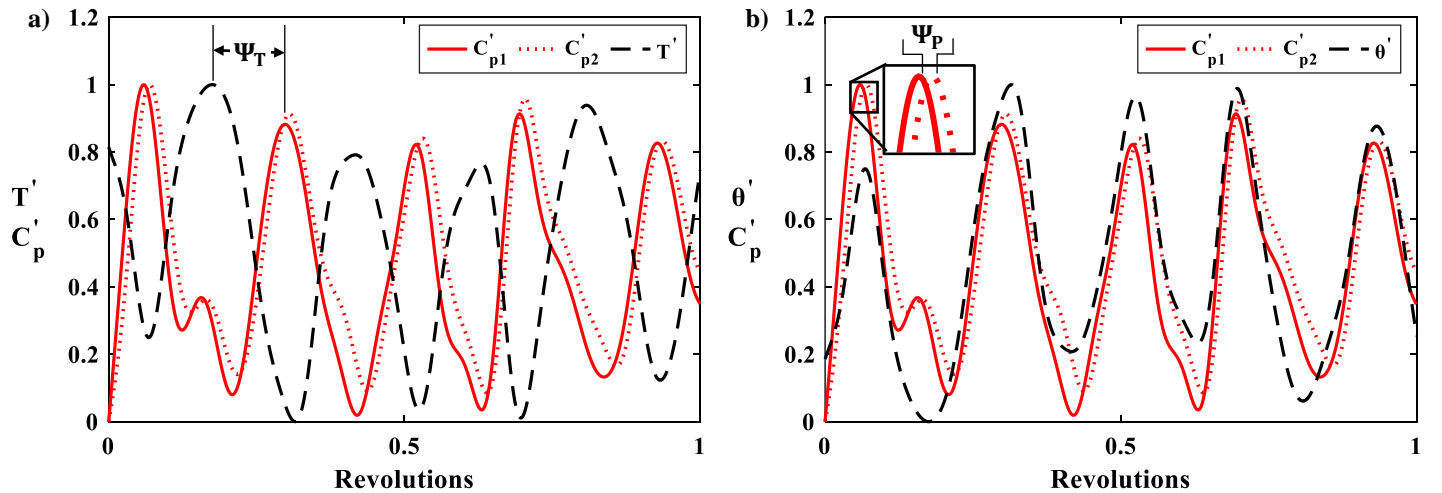


Figure 4: Time trace of normalized parameters at  $PS_b$  case ( $\Phi_p/\Phi_{ref} = 0.86$ ) and  $\Phi_{VTE}/\Phi_{ref} = 0.4$  a) Temperature and pressure coefficient over a single revolution b) Thermal efficiency and pressure coefficient over a single revolution.

Figure 5(a) and Figure 5(b) display the discrete Fourier transform (DFT) from the normalized pressure coefficient and temperature respectively as a function of engine order ( $f/f_D$ ). Stems denote the relative phase of the signal at peak frequencies in Figure 5(a) on the right ordinate. Figure 5(b) utilizes identical frequency values from Figure 5(a) to calculate the relative phase values for the normalized temperature. Using the two  $\Psi$  values from Figure 5(a-b), the difference is calculated to correlate pressure to temperature and is denoted as  $\Psi_T$  in Figure 5(c). This analysis is possible due to the cross-correlation theorem.

One advantage of this method over other correlation methods is that  $\Psi_T$  can be computed independently over a range of frequencies, a capability that is highlighted in Figure 5(c). In the range of  $f/f_D = 4$  to  $f/f_D = 7$ , the pressure and temperature are out of phase, indicating unsteady ingestion occurring across this region of frequencies. Correlating in this way provides the critical frequencies driving the performance of the cavity to be separated from those with a minor impact.

The analysis described above was performed for three cases over a range of sealing conditions: NS,  $PS_b$ , and FS as shown in Figure 3. Temperature phase lag,  $\Psi_T$ , for these three different cases is presented in Figure 6 as a function of normalized frequency,  $f/f_D$ . The dashed lines with open symbols represent cases without VTE flow, and the solid lines with closed symbols represent cases with VTE flow.

Some primary conclusions can be drawn from Figure 6. First, at the NS condition,  $\Psi_T$  is less than  $180^\circ$  across all frequencies. This result is not indicative of time-varying ingress. Although ingress occurs at the NS case (as seen through the steady  $\varepsilon_{cc}$  values in Figure 3), time-varying structures do not contribute to the sealing performance at the rim seal plane. Conversely, the  $PS_b$  case (circles in Figure 6), indicates time-varying ingress through temperature and pressure signals that are out of phase. As shown in Figure 4(a-b), this ingress is related to presence of time-resolved pressure fluctuations and will be discussed in detail in the following section. Finally, for the FS case (triangles), there are low-frequency components that contribute to ingestion to a lesser degree, particularly around  $f/f_D = 2$ , but this region shows fewer out-of-phase frequency contributions than the condition in the inflection region. By relating these findings to the steady sealing effectiveness data, the evaluation method highlighted in Figure 6 shows the inflection region exhibits key frequencies that contribute to ingress and help to explain the deviation from simplified models.

Previous experimental studies have coupled unsteady pressure measurements to the appearance of rotating structures in the cavity region, but could not directly link them to cavity ingestion or the thermal performance of the cavity [13]. This missing relation is most apparent in Figure 7 which displays sealing effectiveness measurements taken by Hualca et al. [13]. The purpose of Figure 7 is not to compare the differences from Hualca et al. [13] to the current study, but to showcase that a cavity instability does not necessarily lead to an inflection in sealing effectiveness. Figure 7 presents sealing effectiveness as

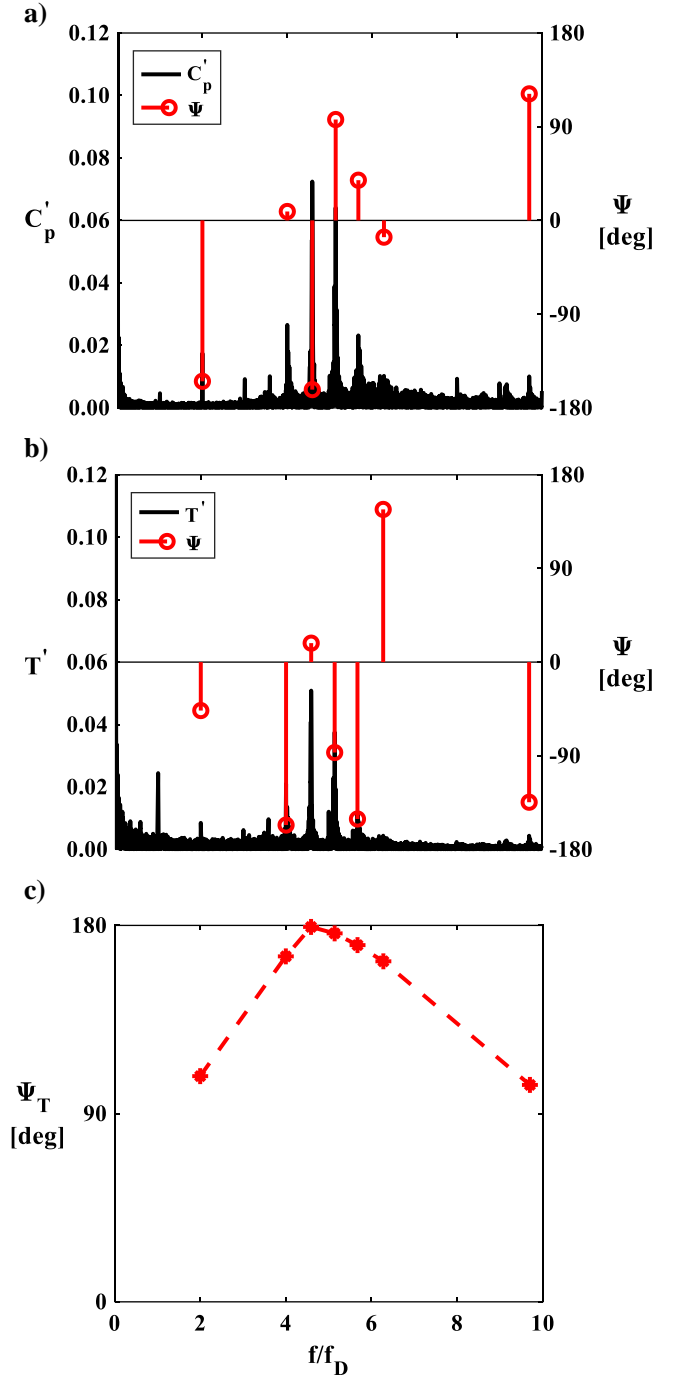


**Figure 5: a) DFT of normalized pressure coefficient and arbitrary phase for peak frequencies. b) DFT of normalized temperature and arbitrary phase for selected frequencies. c) The pressure to temperature phase shift of selected peak frequencies as a function of normalized disc frequency.**



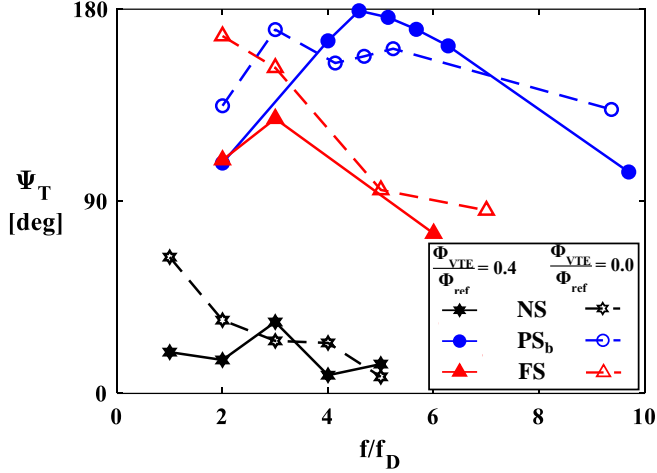


**Figure 6: Lag between pressure and temperature traces as a function of normalized frequency.**

a function of  $\Phi^*$  normalized by the minimum  $\Phi$  value to seal the cavity through

$$\frac{\Phi^*}{\Phi_{\min}} = \frac{\Phi_p - \Phi_{p0}}{\Phi_{\min}} \quad (4)$$

where  $\Phi_p$  is the nondimensional purge flow rate,  $\Phi_{p0}$  is the minimum nondimensional purge flow rate required to start sealing the cavity (accounts for leak paths), and  $\Phi_{\min}$  is the minimum nondimensional purge flow rate required to seal the cavity at the measurement plane. Note, this is different from  $\Phi_{\text{ref}}$  which is the minimum nondimensional purge flow rate required to seal the cavity at the injection plane.

Hualca et al. [13] compares the sealing performance for a double overlap seal with blades (circles) and without blades (triangles). Using high-frequency pressure transducers, Hualca et al. were able to measure time-resolved pressure structures in the cavity for both test cases. However, the sealing effectiveness curve only showed an inflection region in the presence of blades. Thus, even though the pressure structures occur for both conditions, they affect the sealing effectiveness curve in different ways. The interaction of the rotating airfoil in the vane and blade case drives pressure structures to cause ingress. Hualca et al. details that the presence of blades increases the swirl in the cavity creating an instability responsible for the nonmonotonic sealing curve. However, limited details are provided to explain why those structures contribute to ingestion only in the presence of blades and do not create an inflection in the sealing effectiveness curve without blades.

The sealing effectiveness curve for the current study (zero VTE flow case) is also shown in Figure 7 through green squares. In addition, an orifice model [3] was approximately fitted to the current study experimental data using a ratio of discharge coefficients,  $\Gamma=5.2$ . Note that because the orifice model must be monotonically increasing, the model fits the data at low and high  $\Phi^*/\Phi_{\min}$  values, but does not capture the inflection region in the partially sealed region.

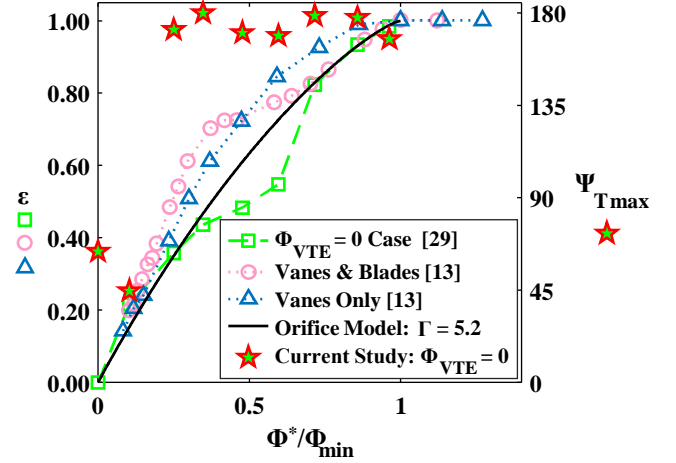


**Figure 7: Sealing effectiveness and phase shift of pressure coefficient to temperature as a function of nondimensional purge flow rate.**

To supplement the sealing effectiveness, the  $\Psi_{Tmax}$  parameter (filled stars), defined as the maximum lag across all frequencies for a particular  $\Phi_p/\Phi_{\text{ref}}$  value is plotted on the right ordinate. In Figure 7, the additional information from a high frequency temperature sensor allows for a classification of nondimensional purge flow rates for which the time-varying events impact sealing effectiveness – a relationship illustrated by the out-of-phase  $\Psi_{Tmax}$  values corresponding to large deviations from the model around the inflection region.

As a corollary, the addition of a high-frequency temperature sensor prevents an incorrect inference that pressure cells cause ingestion from an inflection in steady sealing effectiveness data. In certain cases, such as the vane-only configuration presented by Hualca et al, rotating structures can be present without causing an inflection in the sealing effectiveness. Quantifying  $\Psi_{Tmax}$  through time-resolved pressure and temperature sensors enables coolant rates at which ingestion occurs and the frequencies driving the ingress to be determined. The additional temperature sensor can also relate the existence of pressure structures to the thermal efficiency of the cavity.

## TIME RESOLVED BEHAVIOR IN INFLECTION REGION

The previous section compared NS, PS<sub>b</sub>, and FS cases in Figure 3 claiming that time-resolved pressure and temperature effects contribute to main gas path ingress in the PS<sub>b</sub> region. For this reason, the current section focuses on measurements in the inflection region: PS<sub>a</sub>, PS<sub>b</sub>, and PS<sub>c</sub>. In particular, the relative amplitude of the time-resolved measurements is analyzed. Furthermore, VTE flow is introduced as an additional variable to investigate the impact of the additional coolant on the amplitude of time-varying cavity events.

Discrete Fourier transforms for the three test cases of interest are shown in Figure 8(a-f). These DFTs were computed using the same iterative zero-padding routine described for Figure 5. However, after all cases were computed, the data were normalized by the absolute maximum amplitude across all test

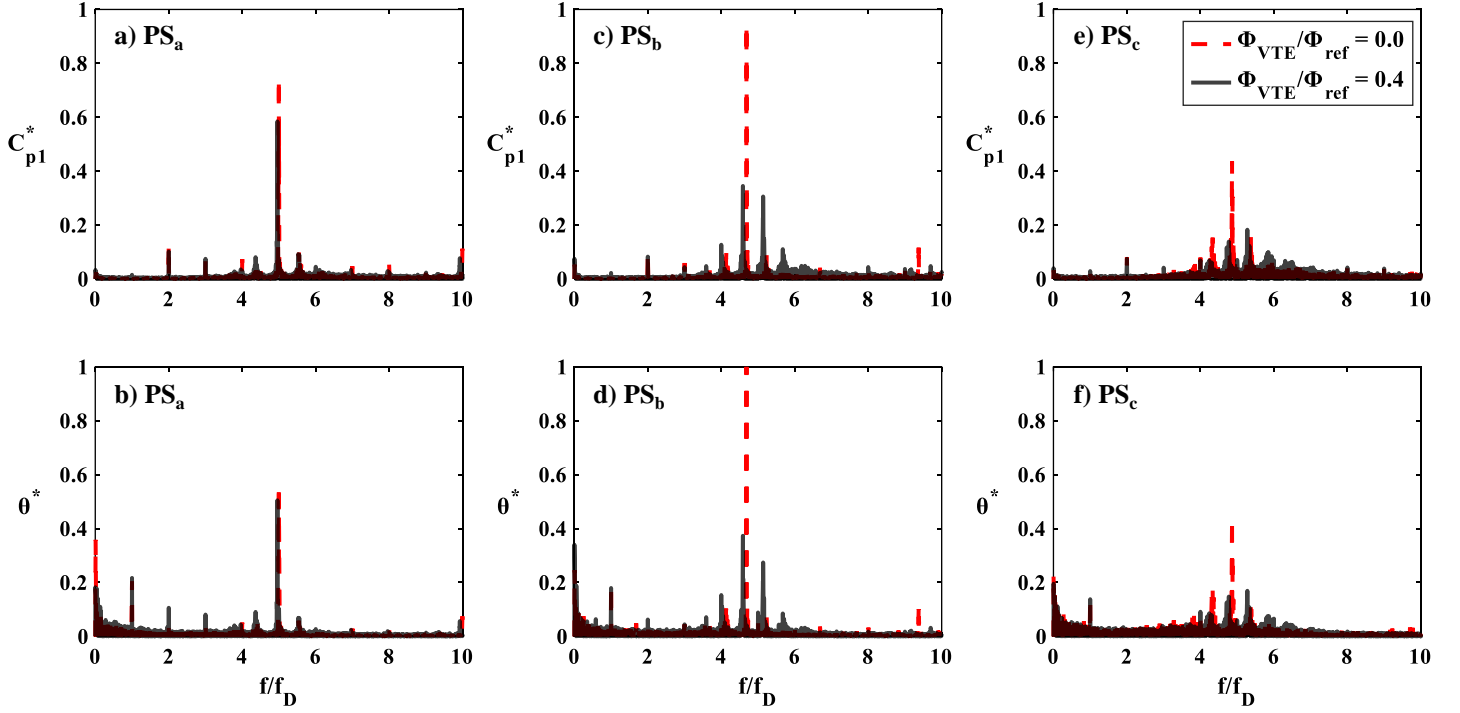


**Figure 8: Discrete Fourier transforms of normalized pressure coefficient and thermal efficiency for inflection region purge flow rates at cases PS<sub>a</sub>, PS<sub>b</sub>, and PS<sub>c</sub>.**

cases. Unlike  $X'$ , which normalized across a single flow condition,  $X^*$  is normalized across all test conditions for relative comparison. For each graph, the dashed lines represent cases without VTE flow, and the solid lines represent cases with VTE flow.

The inflection region data presented in Figure 8(a-f) exhibited the largest amplitude peaks over all evaluated test conditions. Figure 8(a-f) shows that large amplitude values in  $C_p^*$  correspond to large amplitudes in  $\theta^*$ , verifying that these pressure variations are moving pockets of cold and warm air. The experimental data appear as discrete spikes of activity near a normalized frequency of  $f/f_D=5$ . This finding is similar to Hualca et al. who attributed the various peaks to be a fluid instability switching between integer pressure cells [13]. However, in contrast to Hualca et al., no clear relationship between the low frequency spectral peak locations and particular airfoil counts or hardware were identified. More analysis is needed to determine the cause of the frequencies. The effect of VTE on the time-varying events is also evident comparing the peak amplitudes in Figure 8(a-f). Specifically, the VTE flow acts to suppress the time-varying instabilities.

### CORRELATING TIME-RESOLVED MEASUREMENTS WITH COOLING EFFECTIVENESS

The previous section displayed the entire frequency spectra for selected purge flow rates distributed across the inflection region. This section connects time-varying events to cavity

performance indicators by utilizing the maximum amplitude of the frequency spectra.

Figure 9 displays the maximum amplitude normalized cavity efficiency and maximum amplitude normalized pressure coefficient as a function of  $\Phi_p/\Phi_{ref}$ . Additionally, the cooling effectiveness from Figure 3 is provided as an overlay on the graphs for comparison. Figure 9(a) represents a purge-only configuration without VTE flow, whereas Figure 9(b) includes the addition of VTE flow. Furthermore, Figure 9 includes data from three high-frequency sensors (two pressure sensors and one temperature sensor). The independent pressure sensors, which span one fifth of a vane pitch, qualitatively display the same trend and normalized amplitudes illustrating the repeatability and relative insensitivity to circumferential location.

At low  $\Phi_p/\Phi_{ref}$  values in Figure 9, the maximum amplitude of unsteady features is relatively small. This result is consistent with the phase analysis from Figure 6, which showed  $\Psi_T$  does not indicate time-varying ingress at the NS condition. However, when approaching the inflection region (PS<sub>A</sub> and PS<sub>B</sub> in Figure 3), the largest amplitude features are present and have been shown to indicate ingestion. This time-varying ingestion causes the reduction of sealing performance indicative of the inflection point. As  $\Phi_p/\Phi_{ref}$  increases past the inflection point, the time-resolved amplitudes decrease, and the sealing effectiveness returns to a purely increasing behavior. This behavior was also supported by the phase analysis in the FS region (Figure 6).

In both Figure 9(a) and Figure 9(b), the normalized amplitudes reach a peak value coincident with the inflection

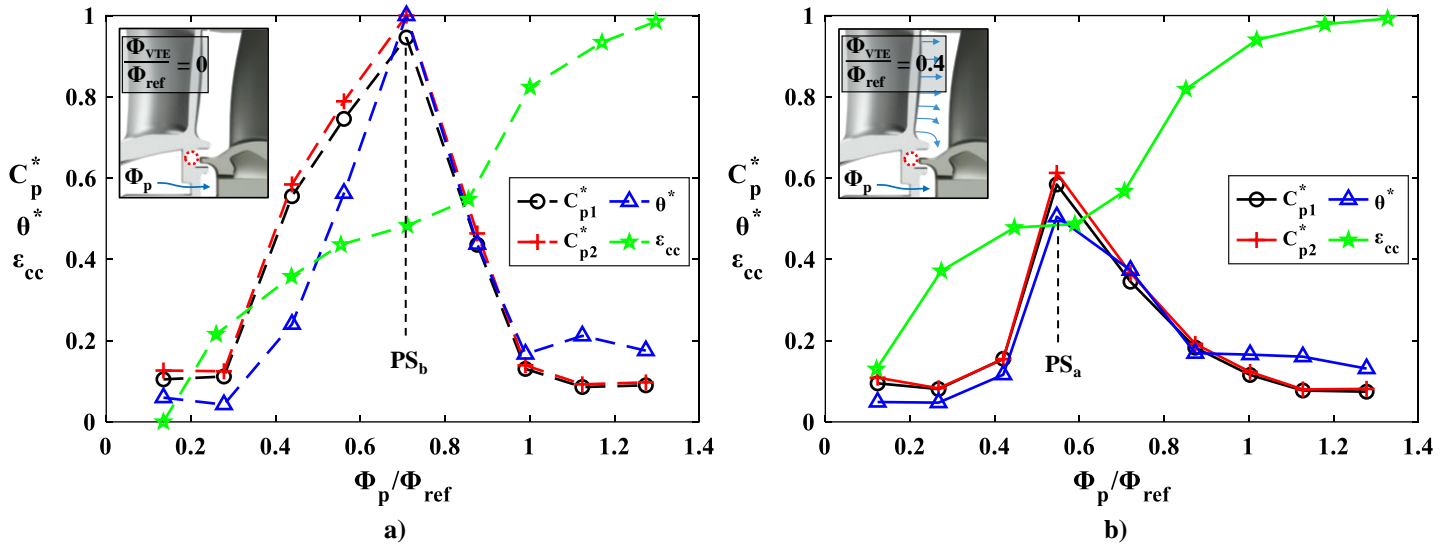


**Figure 9: Max amplitude of normalized pressure coefficient and cavity temperature efficiency plotted with cooling effectiveness across cooling rates. (a) Purge flow only condition,  $\Phi_{VTE}/\Phi_{ref} = 0$ ; (b) Purge flow with the addition of VTE,  $\Phi_{VTE}/\Phi_{ref} = 0.4$ .**

point, as defined by the  $\Phi_p/\Phi_{ref}$  value corresponding to the lowest slope value between neighboring points. Because the inflection point occurs at different nondimensional purge flow rates for the two cases, this finding directly connects the inflection location to maximum unsteady amplitude, not a particular  $\Phi_p/\Phi_{ref}$  value.

Comparing Figure 9(a) to Figure 9(b), the presence of VTE flow also reduces the amplitude of the time-resolved pressure and temperature. Quantitatively, the maximum peak between the two cases is reduced by 50% in the temperature and 40% in the pressure. Interestingly, the inflection of the curve is equally pronounced for both cases, with and without VTE flow, despite the reduction to the unsteady amplitudes. Although this approach of linking a single frequency and amplitude to the sealing effectiveness may be an oversimplification of the complex flow physics present in the rim seal region, it provides a method to connect time-varying events with steady sealing performance. Connections such as these are important to developing real-time turbine health monitoring [30].

## USE OF COMPUTATIONAL MODELING TO SUPPORT EXPERIMENTAL FINDINGS

Computational modeling of engine-realistic geometry can provide insight into the flow physics that are captured by limited measurements in experiments. The purpose of this section is to use CFD simulation results to better understand the experimental measurements previously presented. In particular, a comparison between the  $PS_B$  cases with and without VTE flow will be examined using an Unsteady Reynolds-Average Navier-Stokes (URANS) simulation. A brief description of the URANS approach is provided here for convenience, and further details are outlined by Robak et al. [25].

The computational domain of the turbine stage model consists of a quarter-wheel circumferential sector with cavity flows and engine-realistic leakage paths such as those presented

in Figure 1. The leakage flowrates were set using a 1D pressure network to obtain the mass flow. This domain consists of approximately 22 million elements and employs a pressure-based solver with a  $k-\omega$  SST turbulence model. The geometry represented in the simulation is a direct match for the airfoils and underplatform hardware used in the present study. The simulations were converged to a steady state solution. Then, time-accurate simulations were conducted for five-wheel revolutions before decreasing the time step by a factor of 5 for an additional three-full revolutions. Simulations were considered converged when the pressure amplitude of various tracer points was within 5% of the previous revolution value. Additional details are described in Robak et al. [25].

Although not explicitly presented in this discussion, the time-discrete results confirm low pressure cells rotating around the annulus with number and speed dependent on purge flow rate. When VTE flow is added to the simulation, the strength of these pressure structures decreases, matching the trend in Figure 9. More information about these structures is presented in a complementary study [29].

Time-averaged results representing one full-rotor revolution at the end of the converged period are analyzed here. Figure 10 shows a cross section of the cavity region at a vane phase consistent with the measurement location of  $P_1$  as described in Figure 1 for the case of  $PS_B$  with VTE flow. The contour displays the fraction of VTE flow in the cavity. Note the contour scale in Figure 10 has been reduced to a range from 0 to 0.1 (10% mass fraction) to highlight the trends. As shown previously in Figure 3, the CFD sealing effectiveness was within 7% of experimental values. The added benefit of the simulation allows the individual contributions from VTE and purge flow to be distinguished.

The ingestion of VTE flow identified in Figure 10 further validates the increase in thermal cavity efficiency measured during the experiment and illustrated in Figure 3. This ingestion

occurs in part to a rise in MGP pressure stemming from the additional VTE flow. Because the VTE flow accounts for only two percent of the MGP flow, a majority of the VTE flow is quickly mixed out by the MGP flow. However, near the endwalls, the VTE flow is allowed to propagate further downstream allowing the VTE flow to enter the cavity in relatively high concentrations.

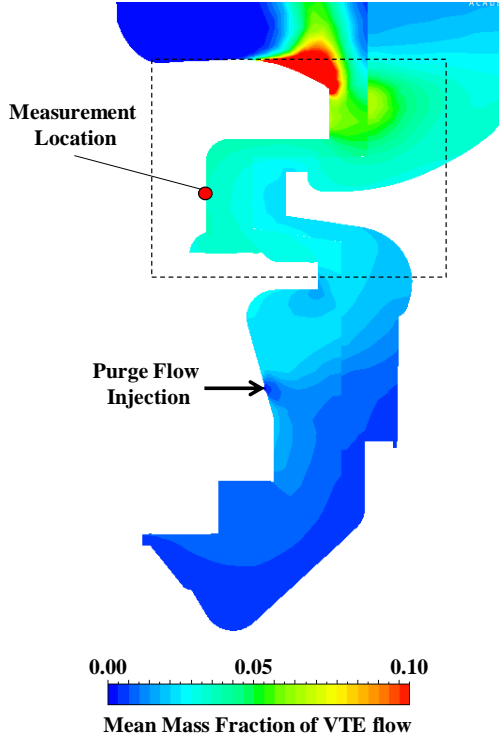


**Figure 10: Contour of VTE ingestion into cavity for PS<sub>B</sub> configuration with VTE flow**

The addition of VTE flow into the cavity changes the fluid dynamics of the cavity leading to suppression of the time-resolved pressure and temperature peaks as seen in Figure 9. To further address this observation, Figure 11 shows contours of swirl ratio for the rim seal region of the cavity (denoted by black dashed box in Figure 10). The swirl ratio is defined as

$$\beta = \frac{V_\phi}{\Omega_D r} \quad (5)$$

where  $V_\phi$  is the tangential velocity,  $r$  is the radial location, and  $\Omega_D$  is the angular speed of the disk. The swirl ratio has been previously identified as a useful parameter for locating mismatches in tangential velocity that could lead to formation of instabilities [31]. In the axial space between the vane and blade in the MGP, the swirl ratio is greater than unity. Physically, the air downstream of the vane must be moving with a tangential velocity capable of spinning the rotor. However, in this study where discrete coolant holes inject air axially into the cavity, there is a large discrepancy between the swirl ratio in the MGP and the cavity region.

Previous authors have shown the velocity gradient is a key driver of Kelvin-Helmholtz instabilities [32]. Because the rim seal of the cavity acts as a buffer region of intermediate swirl ratio separating the MGP from the injection plane, it is of critical importance to instability formation. In Figure 11, there is an increase in the mean swirl ratio with the addition of VTE flow caused by high-swirl VTE fluid propagating downstream near the hub end wall. Because the cavity velocity profile is bounded by the high swirl ratio of the MGP and the axial purge flow injection (zero swirl), the increased swirl ratio stemming from VTE flow ingestion lowers the velocity gradient throughout the cavity and therefore the instability potential. For this reason, the addition of VTE flow suppresses the instability strength and causes the onset of the VTE flow instability to shift relative to the non-VTE case.

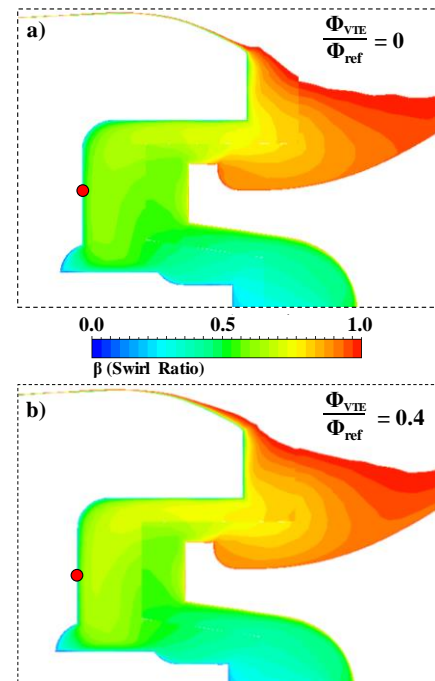


**Figure 11: The mean  $\beta$  for a) purge only condition and b) purge flow with VTE**

## CONCLUSION

This study utilized a single-stage turbine operating with true-scale engine hardware at relevant operating conditions to quantify the effect of coolant flows on the performance of the rim seal region. The steady and time-resolved sealing behavior was quantified using high-frequency pressure and temperature sensors. These data were then compared with CO<sub>2</sub> tracer gas cooling effectiveness measurements for identical conditions.

The comparison of time-resolved measurements with traditional tracer gas sealing quantification shows that VTE flow is ingested into the cavity and measured an increase in the cavity thermal efficiency to be 7-10% with expected contributions from conduction and convection effects. This finding confirms that VTE provides a thermal benefit to the cavity and should be

accounted for in cavity effectiveness modelling to prevent excess use of purge flow.

Correlation of the pressure coefficient and normalized temperature signals indicate ingress occurs when the two signals are out of phase. This method allows separation of time-varying events responsible for ingestion from those less detrimental to cavity performance. For this dataset, it was shown that nondimensional purge flow rates near the cooling effectiveness inflection region create a fluid instability responsible for time-varying ingestion.

A Fourier transform analysis of normalized thermal efficiency and pressure coefficient measurements in this inflection region indicate the presence of low frequency pressure and temperature peaks corresponding to rotating cells in the cavity. The amplitude of these peaks was suppressed by as much as 50% when VTE was present. Using computational simulations, it was shown that the VTE ingestion affects the swirl ratio in the cavity which changes the velocity profile near the rim seal. Because Kelvin-Helmholtz instabilities arise with high velocity gradients, the ingested high-swirl VTE reduces the velocity gradient in the rim seal, suppressing the instability strength. Likewise, swirled coolant could also be used to reduce the velocity gradient.

The maximum normalized amplitude from the spectral analysis was related to the cooling effectiveness where the peak value coincides with the inflection point in the sealing effectiveness curve. This coupling confirms that these unsteady pressure and temperature events are driving time-varying ingress which, in turn, affects the steady sealing performance. Further, at low and high purge flow rates outside the sealing effectiveness inflection region, these time-varying events are partially suppressed. Comparisons with a well-defined ingress model shows that the inflection region deviated from predicted trends in locations where this time-varying behavior is most prevalent.

Overall, the results of this study provide valuable information about how cavity instabilities can drive ingestion under certain conditions and how VTE flow affects cavity performance and the onset of instabilities. This work shows novel application of temperature measurements to provide previously unknown relationships between cavity instabilities and sealing performance. Further, this work elicits research to predict the onset of the instabilities and develop design tools that work to mitigate their effects.

## ACKNOWLEDGEMENTS

The authors would like to recognize and thank Pratt & Whitney and the U.S. Department of Energy National Energy Technology Laboratory under Award Number DE-FE0025011 for supporting research presented in this paper. This report was prepared as an account of work sponsored by an agency of the United States Government. Neither the United States Government nor any agency thereof, nor any of their employees, makes any warranty, express or implied, or assumes any legal liability or responsibility for the accuracy, completeness, or usefulness of any information, apparatus, product, or process disclosed, or represents that its use would not infringe privately

owned rights. Reference herein to any specific commercial product, process, or service by trade name, trademark, manufacturer, or otherwise does not necessarily constitute or imply its endorsement, recommendation, or favoring by the United States Government or any agency thereof. The views and opinions of authors expressed herein do not necessarily state or reflect those of the United States Government or any agency thereof.

## REFERENCES

- [1] Air Transport Action Group, 2018, Aviation Benefits Beyond Borders.
- [2] Bunker, R. S., "Evolution of Turbine Cooling," GT2017-63205.
- [3] Berdanier, R. A., Monge-Concepción, I., Knisely, B. F., Barringer, M. D., Thole, K. A., and Grover, E. A., 2019, "Scaling Sealing Effectiveness in a Stator-Rotor Cavity for Differing Blade Spans," *J. Turbomach.*, **141**(5), pp. 1–10.
- [4] Clark, K., Barringer, M., Johnson, D., Thole, K., Grover, E., and Robak, C., 2018, "Effects of Purge Flow Configuration on Sealing Effectiveness in a Rotor-Stator Cavity," *J. Eng. Gas Turbines Power*, **140**(11), pp. 1–11.
- [5] Johnson, B. V., Mack, G. J., Paolillo, R. E., and Daniels, W. A., "Turbine Rim Seal Gas Path Flow Ingestion Mechanisms," AIAA 94-2703.
- [6] Scobie, J. A., Sangan, C. M., Owen, J. M., and Lock, G. D., 2016, "Review of Ingress in Gas Turbines," *J. Eng. Gas Turbines Power*, **138**(12), pp. 1–16.
- [7] Clark, K., Barringer, M., Thole, K., Clum, C., Hiester, P., Memory, C., and Robak, C., "Using a Tracer Gas to Quantify Sealing Effectiveness for Engine Realistic Rim Seals," GT2016-58095.
- [8] Johnson, B. V., Wang, C. Z., and Roy, R. P., 2008, "A Rim Seal Orifice Model with Two Cd's and Effects of Swirl in Seals," GT2008-50650.
- [9] Johnson, B. V., Jakoby, R., Bohn, D. E., and Cunat, D., 2009, "A Method for Estimating the Influence of Time-Dependent Vane and Blade Pressure Fields on Turbine Rim Seal Ingestion," *J. Turbomach.*, **131**(2), pp. 1–10.
- [10] Hills, N. J., Chew, J. W., and Turner, A. B., 2002, "Computational and Mathematical Modeling of Turbine Rim Seal Ingestion," *J. Turbomach.*, **124**(2), pp. 306–315.
- [11] Sangan, C. M., Pountney, O. J., Zhou, K., Wilson, M., Michael Owen, J., and Lock, G. D., 2012, "Experimental Measurements of Ingestion Through Turbine Rim Seals-Part I: Externally Induced Ingress," *J. Turbomach.*, **135**(2), pp. 1–10.
- [12] Sangan, C. M., Pountney, O. J., Zhou, K., Owen, J. M., Wilson, M., and Lock, G. D., 2012, "Experimental Measurements of Ingestion Through Turbine Rim Seals-Part II: Rotationally Induced Ingress," *J. Turbomach.*, **135**(2), pp. 1–9.
- [13] Hualca, F. P., Horwood, J. T. M., Sangan, C. M., Lock, G. D., and Scobie, J. A., 2020, "The Effect of Vanes and Blades on Ingress in Gas Turbines," *J. Eng. Gas Turbines Power*, **142**(2), pp. 1–12.
- [14] Bohn, D., Rudzinski, B., Sürken, N., and Gärtner, W., "Influence of Rim Seal Geometry on Hot Gas Ingestion into the Upstream Cavity of an Axial Turbine Stage," 99-GT-248.
- [15] Bohn, D., Johann, E., and Kruger, U., "Experimental and Numerical Investigation in Rotor-Stator Systems with Superimposed Coolant Mass Flow," 95-GT-143.
- [16] Bohn, D., Rudzinski, B., Surken, N., and Gartner, W.,

- “Experimental and Numerical Investigation of the Influence of Rotor Blades on Hot Gas Ingestion into the Upstream Cavity of an Axial Turbine Stage,” 2000-GT-284.
- [17] Bohn, D. E., Decker, A., Ma, H., and Wolff, M., “Influence of Sealing Air Mass Flow on the Velocity Distribution in and inside the Rim Seal of the Upstream Cavity of a 1.5-Stage Turbine,” GT2003-38459.
- [18] Cao, C., Chew, J. W., Millington, P. R., and Hogg, S. I., 2004, “Interaction of Rim Seal and Annulus Flows in an Axial Flow Turbine,” *J. Eng. Gas Turbines Power*, **126**(4), pp. 786–793.
- [19] Beard, P. F., Gao, F., Chana, K. S., and Chew, J., 2017, “Unsteady Flow Phenomena in Turbine Rim Seals,” *J. Eng. Gas Turbines Power*, **139**(3), pp. 1–10.
- [20] Horwood, J. T. M., Hualca, F. P., Wilson, M., Scobie, J. A., Sangan, C. M., and Lock, G. D., “Unsteady Computation of Ingress through Turbine Rim Seals,” GT2018-75321.
- [21] Rabs, M., Benra, F. K., Dohmen, H. J., and Schneider, O., “Investigation of Flow Instabilities near the Rim Cavity of a 1.5 Stage Gas Turbine,” GT2009-59965.
- [22] Patinos, M., Ong, I. L., Scobie, J. A., Lock, G. D., and Sangan, C. M., 2019, “Influence of Leakage Flows on Hot Gas Ingress,” *J. Eng. Gas Turbines Power*, **141**(2), pp. 1–11.
- [23] Darby, P. W., Mesny, A. W., De Cosmo, G., Carnevale, M., Lock, G. D., Scobie, J. A., and Sangan, C. M., “Conditioning of Leakage Flows in Gas Turbine Rotor-Stator Cavities,” GT2020-14308.
- [24] Barringer, M., Coward, A., Clark, K., Thole, K. A., Schmitz, J., Wagner, J., Alvin, M. A., Burke, P., and Dennis, R., “The Design of a Steady Aero Thermal Research Turbine (START) for Studying Secondary Flow Leakages and Airfoil Heat Transfer,” GT2014-25570.
- [25] Robak, C. W., Faghri, A., and Thole, K. A., “Analysis of Gas Turbine Rim Cavity Ingestion with Axial Purge Flow Injection,” GT2019-91807.
- [26] Monge-Concepción, I., Berdanier, R. A., Barringer, M. D., and Thole, K. A., 2019, “Evaluating the Effect of Vane Trailing Edge Flow on Turbine Rim Sealing,” *Journal of Turbomachinery*, American Society of Mechanical Engineers, pp. 1–14.
- [27] Siroka, S., Berdanier, R. A., Thole, K. A., Chana, K., Haldeman, C. W., and Anthony, R. J., 2020, “Comparison of Thin Film Heat Flux Gauge Technologies Emphasizing Continuous-Duration Operation,” *J. Turbomach.*, **142**(9), pp. 1–10.
- [28] Wang, C. Z., Mathiyalagan, S. P., Johnson, B. V., Glahn, J. A., and Cloud, D. F., 2013, “Rim Seal Ingestion in a Turbine Stage from 360 Degree Time-Dependent Numerical Simulations,” *J. Turbomach.*, **136**(3), pp. 1–12.
- [29] Monge-concepción, I., Siroka, S., Berdanier, R. A., Barringer, M. D., Thole, K. A., and Robak, C., “Unsteady Turbine Rim Sealing and Vane Trailing Edge Flow Effects,” GT2021-59273.
- [30] DeShong, E. T., Peters, B., Berdanier, R. A., Thole, K. A., Paynabar, K., and Gabraeel, N., “Correlating Time-Resolved Pressure Measurements with Rim Sealing Effectiveness for Real-Time Turbine Health Monitoring,” GT2021-59586.
- [31] Horwood, J. T. M., Hualca, F. P., Wilson, M., Scobie, J. A., Sangan, C. M., Lock, G. D., Dahlqvist, J., and Fridh, J., 2020, “Flow Instabilities in Gas Turbine Chute Seals,” *J. Eng. Gas Turbines Power*, **142**(2), pp. 1–12.
- [32] Gramer, L., 2007, Kelvin-Helmholtz Instabilities GFD-II, (May).